Journal of
Synchrotron Radiation

ISSN 0909-0495

Received 28 December 2006
Accepted 12 April 2007

Are you centered? An automatic crystal-centering method for high-throughput macromolecular crystallography

Anubhav Jain[a] and Vivian Stojanoff[b]*

[a]Department of Materials Science and Engineering, Massachusetts Institute of Technology, Cambridge, MA 02139, USA, and [b]Brookhaven National Laboratory, Upton, NY 11973, USA. E-mail: vivian.stojanoff@gmail.com

Crystal centering is a key step in macromolecular X-ray crystallography experiments. A new method using image-processing and machine-vision techniques allows the centering of small crystals in the X-ray beam. This method positions crystals even when the loop is initially out of the camera's field of view and adapts to the difficulty of the experiment. The process has been tested on many diverse crystals with a 93% success rate when compared with manual centering.

Keywords: automated crystal centering; computer vision; robotic automation techniques; high-throughput crystallography; X-ray diffraction; protein crystallography.

1. Introduction

In recent years, better synchrotron sources and modern detectors have drastically reduced the time needed to perform macromolecular crystallography experiments. With data collection now taking only a few minutes at third-generation machines, the 5–20 min traditionally spent for manually mounting and centering the sample has become unacceptable (Leslie *et al.*, 2002). Quick set-up is even more essential in high-throughput experiments that require the analyses of a large number of crystals. In these experiments, crystal centering can compose most of the total experimental time.

At most synchrotron facilities, robotic elements have been or are being incorporated to reduce the time needed to perform an experiment. The ultimate use of automation, however, would be a fully computer-controlled macromolecular crystallography experiment. This system would be able to mount, center, diffract and check the quality of a crystal without any human intervention. With this system, crystal screening projects would become immensely more practical, experiments could run non-stop at all hours, and researchers using these facilities would require less time from local researchers. Significant progress towards this goal has already been made at several beamlines with the integration of fully functional automatic sample changers and mounters (Pohl *et al.*, 2004; Snell *et al.*, 2004; Ohana *et al.*, 2004; Cipriani *et al.*, 2006). Automatic crystal quality analysis based on initial diffraction data is also being developed (Berntson *et al.*, 2003; Zhang *et al.*, 2006). However, crystal centering remains a bottleneck in the process.

Several research groups have demonstrated a partial solution to the sample-centering problem by automatically centering the loop containing the crystal. This has been achieved in several different ways, including contour extraction (Roth *et al.*, 2002) and loop recognition masks (Karain *et al.*, 2002). These methods will be successful when the size of the crystal is comparable with the size of the loop and when the crystal is near the center of the loop. However, if left unassisted they will fail in other cases, and therefore do not allow for a fully automated data collection setting.

There are only a few published reports on automatic crystal centering. Though showing some promising data, the performances of these techniques were not quantitatively reported and many groups are working on improving these methods (Muchmore *et al.*, 2000; Andrey *et al.*, 2004; Pothineni *et al.*, 2006). Several groups have attempted to use UV fluorescence techniques to better image the crystal for centering (Jacquamet *et al.*, 2004; Pohl *et al.*, 2004; Vernede *et al.*, 2006). However, fluorescence visualization has several drawbacks, including the need for special equipment, a UV source, special optics to maximize the signal, and non-fluorescent loops; the need for experimental set-up space and safety issues; low fluorescence signal from many proteins, and crystal radiation damage issues associated with a UV laser (Vernede *et al.*, 2006). Furthermore, the use of such a UV system has not been shown to lead to a consistently accurate centering routine.

In this report we describe the development of a fully automated crystal-centering method that allows for the accurate positioning of a macromolecular crystal in the X-ray beam. No initial information on the sample or experimental

setting are necessary, nor are any constraints applied. When used in conjunction with an automatic sample changer/mounter, this method allows the performance of a fully automated experiment from crystal alignment in the X-ray beam to data collection.

2. The experimental environment

The typical experimental environment used in a macromolecular crystallography X-ray diffraction experiment consists of a rotation axis and a small centering table that carries the crystal holder. Usually a microscope attached to a charged coupled device (CCD camera) positioned at 90° or 45° from the spindle axis allows the visualization of the sample; light is provided by a single optical fiber through a condenser. A cryogenic sample conditioner maintains the sample under a constant flow of cold nitrogen gas.

The crystal-centering method proposed in the current report is suitable for any experimental set-up with the characteristics described above. It was developed specifically for the experimental environment at the X6A beamline (NSLS) (Fig. 1), which consists of a Crystal Logic diffractometer and a small XYZ centering table, also Crystal Logic, a sample cryocooler (Oxford Instruments, series 700) and an Advanced Light Source automatic sample mounter (Snell *et al.*, 2004). The single rotation axis is powered by a step motor, 200 steps per degree, and the XYZ centering table allows for *xyz* translations of approximately 1 µm per microstep and limited K movements. The sample environment further contains a prism that can be automatically positioned in-line with the beam during sample set-up and retracted during data collection, allowing a black-and-white CCD camera, positioned below the crystal, to image the sample along the beam path (R. Nordmeyer, E. Cornell, D. Yegian & T. Earnest, private communication). The camera is set up with computer-controlled microscope zoom lenses and focus (Navitar 12× Ultrazoom). The sample is backlit using a system of five LEDs fed through a diffuser screen, which provides uniform background illumination and prevents glare.

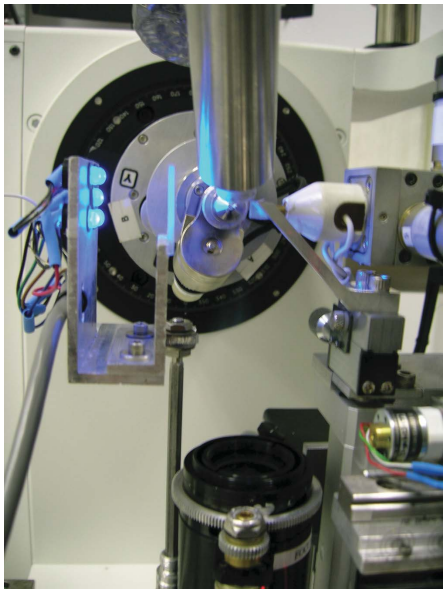

Figure 1
Close-up view of the X6A beamline experimental setting.

BluIce-like software [Distributed Control System (DCS) (Snell *et al.*, 2004; McPhillips *et al.*, 2002)] is used for sample set-up and data collection. DCS controls all diffractometer motors and communicates with the monochromator motor, allowing for custom protocols including the automounter and centering hardware. With this software it is possible to automatically analyze, mount, center and diffract up to 64 samples at a time, the full capacity of the X6A automounter.

3. The crystal auto-centering method

Macromolecular crystals can grow in many different shapes but are usually small in size, 80 to 200 µm on average. Most crystals are transparent, although colored or opaque crystals are not unusual. This large variety in size and shape makes it impossible to find any positioning method on the search of a signature pattern. The method proposed here is based on image-processing and machine-vision techniques. It consists of three steps. In the first the loop is centered at low magnification, followed by a second step in which the loop is centered at high magnification; for the results presented in §4, low and high magnification differed by a factor of six. In the final step the crystal is positioned in the beam center at high magnification.

Frequently, when mounted on the diffractometer, the loop, and consequently the crystal, is not even in the field of view of the camera. Pre-centering of the loop at low magnification brings it to the optics' focal position and very roughly positions it to the beam center position so that it can be accurately centered at a higher magnification. In this step, image processing is used to detect and center the loop so that it comes into focus. If initially the loop is not in the camera's field of view, a sequence of alternate rotations and translations is executed until an image of the loop can be detected. If the loop is not found after four iterations, the method will abort, as it is likely that there is no loop mounted on the diffractometer. Otherwise, it will continue with the centering procedure, having located the loop successfully.

Once the loop is detected, its center is calculated and the loop center is moved to the position of the beam. To ensure that the movement was executed successfully, the loop is re-detected. Specifically, the algorithm checks whether the loop can now be detected at the beam position. If this confirmation fails, the loop is moved again to the beam center and checked. If the confirmation succeeds, the centering process is repeated for four ω angles, 90° apart, to ensure accuracy and three-dimensional centering.

Sometimes the loop is very far from the focal position of the camera and only the pin carrying the loop can be seen as a blurry image (Fig. 2). In these cases shape analysis is performed to automatically recognize that only the pin has been detected. The number of rotation-and-translation iterations mentioned above is immediately adjusted from four to

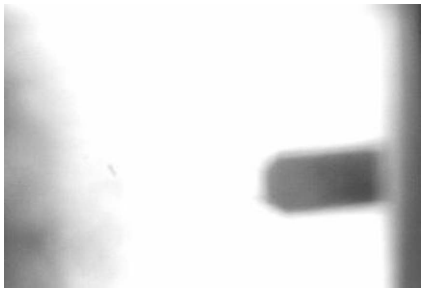

Figure 2
An image in which the loop is not visible in the camera field of view; only the blurry image of the pin that carries the loop is visible. The centering method discussed in the text can adapt to this situation by increasing the number of iterations used in the process. The loop comes into focus during the later iterations, allowing for proper centering. (Field of view: 4.2 mm × 2.9 mm.)

eight to increase centering accuracy for this difficult scenario. During the first three or four iterations, the pin edge is brought into the beam center, bringing the loop into focus. Once the loop becomes visible, the subsequent iterations will center the loop. The number of iterations is also increased to eight if the loop rotates out of the field of view of the camera or when the pin carrying the loop spans the entire image. In the case where no loop is visible in the camera's field of view, a series of translations and ω-axis rotations are used to find the loop-pin as described previously. By adjusting the behavior of the pre-centering process to specific cases, the method presented here simulates the actions of researchers during an experiment. The pre-centering time therefore varies and, as for manual alignment, depends on how well aligned the loop is at the start.

Following the pre-centering step the same protocol is used to ensure that the loop is centered at high magnification. This stage ensures that optimal focus is attained for crystal centering. As for the low-magnification case, contrast enhancement and image processing assure that the loop is centered in four to eight steps by combining 90° rotations in ω and xyz translations of the small translation table.

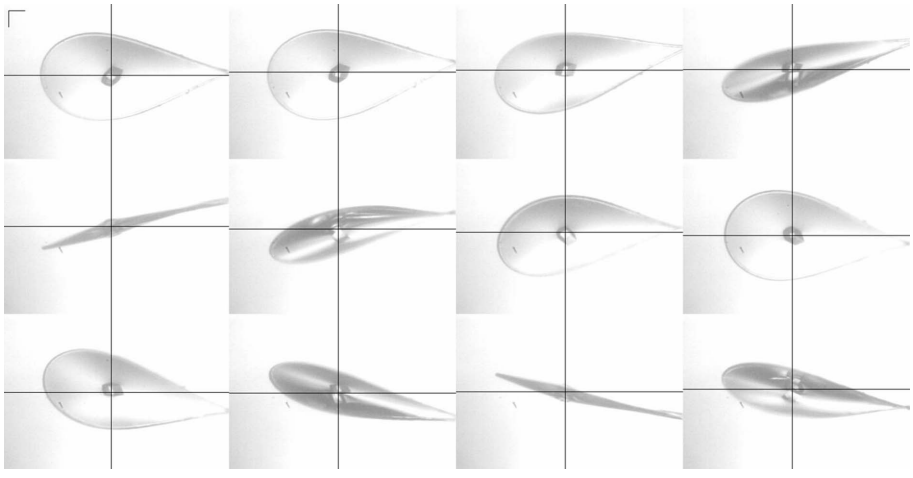

Figure 3
The composite image created at the final stage of crystal centering shows the centered sample in 12 positions 30° apart. The performance of the crystal-centering process can be quickly, easily and accurately verified through these images. Scale bars on the top-left corner correspond to 100 μm. (Field of view: 1.8 mm × 1.2 mm.)

At the final stage the crystal is centered at high magnification. Twelve images of the centered loop at 30° rotation intervals are analyzed. Filters and noise reduction are applied, as will be described in §3.2, to give the best estimate of the crystal position. Following the translation of the crystal to the beam center, a combination of two translations of the small XYZ table, 90° apart from each other, assure that the crystal is centered in three dimensions with relation to the X-ray beam. In addition, a composite image with the detected crystal position at all 12 rotation angles (Fig. 3) allows for a visual analysis of the crystal-centering process afterwards.

3.1. Loop detection

The loop detection process follows a basic standard-deviation analysis of intensity of each pixel in the image and is combined with an edge filter procedure. Prior to the analysis, the image is submitted to a contrast-enhancement step that minimizes background illumination dependence. In the standard-deviation analysis each pixel is replaced by the standard deviation of the intensity calculated in a 7×7 window centered on that pixel. A Sobel edge filter (Davies, 1997) allows the reliable location of the loop even when the image is very blurry, since the standard deviation in a large window changes greatly near the loop edges. Once the loop edges are found, a threshold is determined to eliminate background noise and to correct for undetected edge pixels. This procedure effectively separates the background from the loop object (Fig. 4) and smoothens out the loop shape. In a final step, the loop pin and loop handle are eliminated from the image through shape analysis. This leaves only the loop in the image (Fig. 4).

3.2. Crystal detection

The crystal is detected in two stages. In the first, each image is individually preprocessed to detect crystal edges and corners inside the loop, providing a preliminary notion of the crystal location in each image. In the second, the information from the 12 rotation images is combined to reject spurious data and form a dynamic view of the crystal position during rotation.

The preprocessing step consists of the determination of the loop position in the high-magnification image, as described earlier. Using a simple erosion filter the loop fiber is eliminated from the image by zeroing every pixel on the edge of the loop. The filter is applied until the totality of the loop thickness has been removed. A median edge/corner detector filter (Paler *et al.*, 1984; Davies, 1988) is then used to search inside the loop region for edges and corners that should pertain to the crystal. This filter gives a strong response to edges and an even stronger

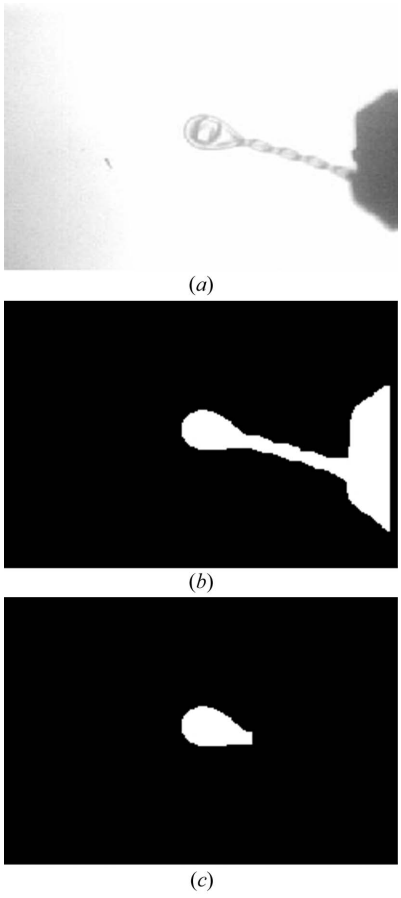

Figure 4
Loop-recognition procedure. (*a*) The original image at high magnification. (*b*) In the image-processing step, the background is separated from the foreground, with the loop pin and handle still remaining. (*c*) Shape analysis allows the loop to be isolated from the rest. The center of this region is calculated as the loop center.

response to corners, compared with other edge filters (Davies, 1997; Canny, 1986; Smith & Brady, 1997). It is also shown to be robust to lighting effects so frequently encountered during the manual crystal-centering process. The preprocessing stage is completed by defining a threshold to the output of the median edge/corner detector.

In the second stage, the preprocessed edge and corner information of each image are combined. To minimize lighting effects, only eight images (those that present the largest loop sizes) are superimposed to form a so-called 'total' image (Fig. 5). It is important to note that the crystal center does not change along the rotation axis (horizontal axis in the image) but follows a vertical line segment during rotation. Therefore by combining the rotation images the crystal outline can be estimated from the vertical smear present in the 'total' image. Noise and lighting effects would not produce this characteristic smear as they would not follow a predictable pattern during rotation. The degree of smear for each position along the horizontal axis is calculated as the sum of intensities of all pixels along the vertical direction at a given position. This information is graphically represented on the 'total' image (Fig. 5) as a horizontal bar at the bottom of the figure. This horizontal bar varies in intensity along the rotation axis, with regions of high smear being represented by the whiter regions (more intensity) compared with those that correspond to low smear. At this stage all pixels corresponding to low-smear regions in all images are zeroed except those pixels that fall in between two sections of high smear, as these two high-smear sections are taken as the left and right limits of the crystal edge.

Following this noise-reduction step, the centroid of the remaining edge points is estimated for each of the preprocessed images. Along the rotation axis the crystal center will be given by the median of the centroids as the crystal center is expected not to change along the horizontal axis in the image. However, for the vertical direction it is not possible to take the median of the centroid values as the vertical position of the crystal center is expected to be different for different rotation

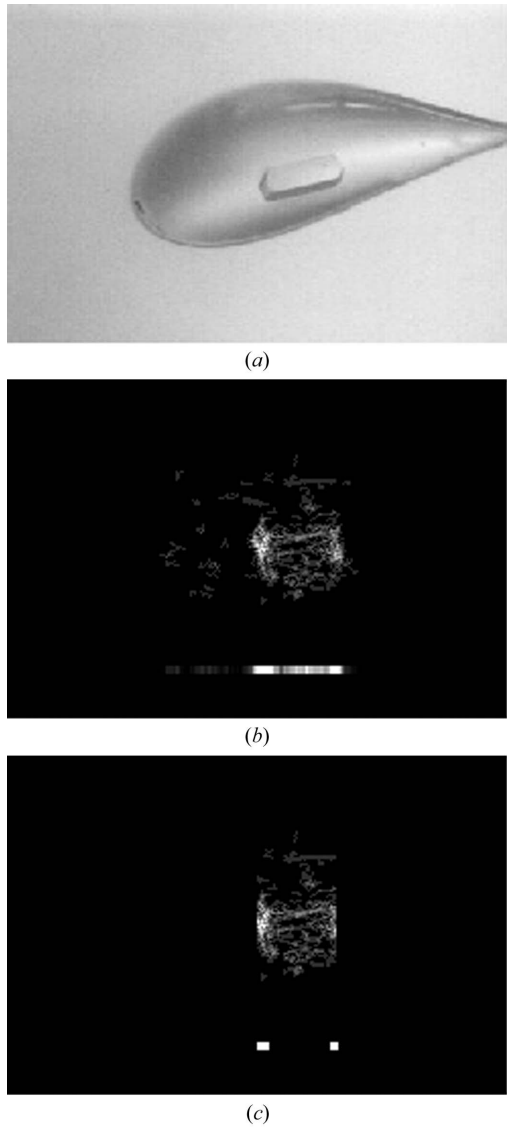

Figure 5
Crystal detection. (*a*) A high-magnification image of the sample at a specific rotation angle. (*b*) Superposition of the combined raw edge information of the sample at all angles. The horizontal bar at the bottom shows the intensity of the image integrated in the vertical direction, or degree of smear. (*c*) To reduce noise, pixels which are not contained between regions of high smear are zeroed.

Table 1
Performance of the crystal-centering algorithm upon automated positioning of 100 crystals (set I) and 54 crystals (set II).

Following the first criteria the crystal center for samples classified in the well centered category was within 50 μm of the beam central position, and for crystals in the average class within 100 μm. Set II is part of a crystal screening experiment for best diffraction and data collection.

Classification	Crystal set I (%)	Crystal set II (%)
Well centered	75.8	77.9
Average	20	17.9
Poor	4.2	4.2

angles. Instead, the position of the crystal center is obtained by fitting the projections of the vertical coordinates from each rotation image onto a circle. Rather than using the Nelder–Mead simplex optimization (Andrey *et al.*, 2004), the optimal fit is solved algebraically, yielding smaller computational times. This fitting procedure is repeated three times as not all data points agree with the initial fit and are discarded before the fit is recalculated. In the final fitting step the information from the four images which presented the smallest loop sizes are included.

Following this analysis the crystal center position is re-generated at all rotation angles as best described by the fit. The dynamic view of the crystal position at all rotation angles permits the crystal center to be positioned in the beam.

4. Results

The results from two different sets of crystals have been analyzed. The first set consisted of 100 crystals mounted on the diffractometer either manually or by an automated sample changer. Forty crystals in this set were standard tetragonal hen egg-white lysosyme crystals, and the remaining 60 crystals were provided by researchers of the X6A beamline. The second set contained 54 crystals, corresponding to nine different proteins, which were mounted on the diffractometer by the X6A automated sample changer. The first set was aimed to study the accuracy of the method when exposed to the large variety of macromolecular crystals of different shapes and sizes. The second set was collected during an actual crystal screening experiment. The effectiveness of the method was analyzed following two different criteria with a success rate of the order of 93%. The efficiency was also analyzed as a function of image quality and is discussed below in relation to computer and beamline hardware.

4.1. Accuracy results

The centering results have been classified according to two different criteria as suggested in the literature (Pothineni *et al.*, 2006; Lavault, 2006). For the first criteria, three categories were considered: 'well centered', 'average' and 'poor'. Crystals classified in the well centered category were those in which the crystal center was positioned within 50 μm of the beam center at all rotation angles. Crystals that fell into the average category were those for which the center was found within 100 μm of the beam center at all rotation angles. For crystals classified in the poor category the crystal center was off by more than 100 μm from the beam center. Following this classification, 95% of the crystals analyzed from the first set fell into the well centered and average categories (Table 1). These results were reproduced extremely well for the second set of crystals collected during an actual crystal screening experiment. This set also shows 96% of crystals as classified in the well centered or average categories, and differs from the first only in that more crystals were found in the well centered category than for the first crystal set. Finally, the image sets for which even manual inspection did not allow the visualization of the crystal were classified as 'unsolvable'; about 5% for both sample sets was classified as unsolvable.

Table 2
Performance of the crystal-centering algorithm upon automated positioning of 100 crystals (set I) and 54 crystals (set II).

Following the second criteria, the crystal center for samples classified in the well centered category was positioned on the beam center within the experimental error, and for crystals in the average class the beam was centered on one of the edges of the crystal. Set II is part of a crystal screening experiment for best diffraction and data collection.

Classification	Crystal set I (%)	Crystal set II (%)
Well centered	67.4	74.2
Average	27.4	19.4
Poor	5.3	7.5

One intrinsic problem with the criteria described above is the rather arbitrarily chosen distance between crystal center position and the beam center. The values of 50 and 100 μm seem to match well the crystals and the experimental setting on the X6A beamline, although crystal sizes of the order of 50 μm are not that rare. Therefore both sample sets were reclassified following a second criterion for which the crystal is said to be 'well centered', when the crystal center coincides with the beam position, 'average', when one edge of the crystal is still grazed by the beam, or 'failed'. Using this criterion, about 90% of the crystals were classified within the well centered and average categories (Table 2). Following this criterion the success rate for smaller crystals was found to be higher then for larger crystals. This can be explained by considering that for larger crystals often one edge stands out in the image. In this case the method proposed here often just finds this edge and centers it on the beam. For smaller crystals usually all edges are visible, and even if only one edge is found and centered on the beam the actual crystal center is close to the edge.

This high success rate observed for both criteria compared with manual centering can be ascribed to the stable performance of the median edge/corner detector as well as to the noise-reduction and curve-fitting procedures employed after image processing.

4.2. Centering speed

In order to test the time spent positioning the crystal center in the beam, the method described in §3 was integrated into the X6A beamline *BluIce*-like graphical user interface. Positioning a crystal in the beam essentially depends on the

Table 3
Percentage of total centering time spent performing various tasks for a 'difficult' centering case in which the loop was originally out of the camera's field of view, even at low magnification.

The total centering time was 5′ 36″. The actual time spent processing the images is less than 1 s per image.

Task	Percentage of time (%)
Moving ω-axis	67
Moving XYZ heads	16
Computing	11
Communicating with camera server	4
Moving camera zoom	2

complexity presented by each crystal and on the hardware being accessed. As is true for researchers centering a crystal manually, times may vary largely (Snell *et al.*, 2004). An initially well centered sample will be positioned much more quickly than one which initially is not in the camera's field of view. The centering procedure using this algorithm takes only a few seconds. Most of the time is actually spent moving motors and communicating with the hardware (Table 3). On a dual Pentium-III 1 MHz Linux workstation, less than 1 s per image is spent performing image analysis. In particular, improving the speed of the ω axis, which currently rotates at a speed of about $6^\circ\ s^{-1}$, by a factor of two would cut the centering time by 33%.

5. Conclusion

The crystal-centering method discussed here allows for high-throughput experiments without human interventions. The method was shown to reliably and accurately center a diverse set of crystals. The automatic centering algorithm, *CrysCent*, has been integrated with DCS under a *BluIce*-like interface both as a 'one-click' button and as a 'no-click' automated experimental step. The algorithm offers unprecedented simplicity and control in programming an automatic experimental protocol as it allows for sample centering even if the loop is initially out of the camera's field of view. Instead of raw images, as used by existing crystal-centering methods, for dynamic image sequence analysis, the proposed method uses preprocessed images. This trait in *CrysCent* allows only significant features in the image to be kept. Furthermore, the inclusion of a loop-aligning step in high magnification helps in the refinement of the overall positioning process. The composite image created in the process serves the double purpose of allowing the refinement of the crystal-centering process as well as allowing researchers to quickly check the centering performance. Used in combination with automated sample changing and diffraction-quality analysis this method allows for unattended data collection at macromolecular crystallography stations at synchrotron facilities.

The assistance of J. Jakoncic, M. Worth, M. Allaire and F. Yokaichiya is greatly appreciated. The input of Earl Cornell enabled the integration of *CrysCent* into DCS. The authors wish to thank D. P. Siddons for valuable suggestions. This research would not have been possible without the expert technical assistance from A. Lenhard, A. Kushewski and B. Clay. One of the authors would like to acknowledge partial funding from the DOE SULI program. The X6A beamline is funded by the NIGMS under contract GM0080. Funding for the NSLS is provided by DOE under contract No. DE-AC02-98CH10886.

The software is available to collaborators: please contact one of the authors, anubhavj@mit.edu or vivian.stojanoff@gmail.com.

References

Andrey, P., Lavault, B., Cipriani, F. & Maurin, Y. (2004). *J. Appl. Cryst.* **37**, 265–269.
Berntson, A., Stojanoff, V. & Takai, H. (2003). *J. Synchrotron Rad.* **10**, 445–449.
Canny, J. (1986). *IEEE Trans. Patt. Anal. Machine Intell.* **8**, 679–698.
Cipriani, F., Felisaz, F., Launer, L., Aksoy, J.-S., Caserotto, H., Cusack, S., Dallery, M., di-Chiaro, F., Guijarro, M., Huet, J., Larsen, S., Lentini, M., McCarthy, J., McSweeney, S., Ravelli, R., Renier, M., Taffut, C., Thompson, A., Leonard, G. A. & Walsh, M. A. (2006). *Acta Cryst.* D**62**, 1251–1259.
Davies, E. R. (1988). *Lect. Notes Comput. Sci.* **301**, 360–369.
Davies, E. R. (1997). *Machine Vision: Theory, Algorithms and Practicalities*, 2nd ed. San Diego: Academic Press.
Jacquamet, L., Ohana, J., Joly, J., Legrand, P., Kahn, R., Borel, F., Pirocchi, M., Charrault, P., Carpentier, P. & Ferrer, J.-L. (2004). *Acta Cryst.* D**60**, 888–894.
Karain, W. I., Bourenkov, G. P., Blume, H. & Bartunik, H. D. (2002). *Acta Cryst.* D**58**, 1519–1522.
Lavault, B. (2006). *C3D: A tool for automated crystal alignment on high throughput macromolecular X-ray beamlines*, http://www.embl-grenoble.fr/groups/instr/auto_centring/index.html.
Leslie, A. G. W., Powell, H. R., Winter, G., Svensson, O., Spruce, D., McSweeney, S., Love, D., Kinder, S., Duke, E. & Nave, C. (2002). *Acta Cryst.* D**58**, 1924–1928.
McPhillips, T. M., McPhillips, S. E., Chiu, H.-J., Coen, A. E., Deacon, A. M., Ellis, P. J., Garman, E., Gonzalez, A., Sauter, N. K., Phizackerley, P., Soltis S. M. & Kuhn, P. (2002). *J. Synchrotron Rad.* **9**, 401–406.
Muchmore, S. W., Olson, J., Jones, R., Pan, J., Blum, M., Greer, J., Merrick, S., Magdalinos, P. & Nienaber, V. L. (2000). *Structure*, **8**, R243–246.
Ohana, J., Jacquamet, L., Joly, J., Bertoni, A., Taunier, P., Michel, L., Charrault, P., Pirocchi, M., Carpentier, P., Borel, F., Kahn, R. & Ferrer, J.-L. (2004). *J. Appl. Cryst.* **37**, 72–77.
Paler, K., Foglein, J., Illingworth, J. & Kittler, J. (1984). *Pattern Recognit.* **17**, 535–543.
Pohl, E., Ristau, U., Gehrmann, T., Jahn, D., Robrahn, B., Malthan, D., Dobler, H. & Hermes, C. (2004). *J. Synchrotron Rad.* **11**, 372–377.
Pothineni, S. B., Strutz, T. & Lamzin, V. S. (2006). *Acta Cryst.* D**62**, 1358–1368.
Roth, M., Carpentier, P., Kaïkati, O., Joly, J., Charrault, P., Pirocchi, M., Kahn, R., Fanchon, E., Jacquamet, L., Borel, F., Bertoni, A., Israel-Gouy, P. & Ferrer, J.-L. (2002). *Acta Cryst.* D**58**, 805–814.
Smith, S. M. & Brady, J. M. (1997). *Intl J. Comput. Vision*, **23**, 45–78.
Snell, G., Cork, C., Nordmeyer, R., Cornell, E., Meigs, G., Yegian, D., Jaklevic, J., Jin., J., Stevens., R. C. & Earnest, T. (2004). *Structure*, **12**, 537–545.
Vernede, X., Lavault, B., Ohana, J., Nurizzo, D., Joly, J., Jacquamet, L., Felisaz, F., Cipriani, F. & Bourgeois, D. (2006). *Acta Cryst.* D**62**, 253–261.
Zhang, Z., Sauter, N. K., van den Bedem, H., Snell, G. & Deacon, A. M. (2006). *J. Appl. Cryst.* **39**, 112–119.